Fluid–structure interactions of skeleton-reinforced fins: performance analysis of a paired fin in lift-based propulsion

Kourosh Shoele and Qiang Zhu*

Department of Structural Engineering, University of California, San Diego, La Jolla, CA 92093, USA

*Author for correspondence (e-mail: qizhu@ucsd.edu)

SUMMARY

We investigate the thrust generation capacity of a thin foil consisting of a membrane strengthened by embedded rays that is geometrically, structurally and kinematically similar to pectoral fins of bony fishes during lift-based labriform locomotion. Our numerical model includes a fully nonlinear Euler–Bernoulli beam model of the skeleton and a boundary-element model of the surrounding flow field. The fin undergoes a dorso–ventral flapping activated by rotations of the rays. Both the trailing edge vortices (TEV) and the leading edge vortices (LEV) are accounted for and modeled as shear layers. The thrust generation and propulsion efficiency are examined and documented. Our results show that synchronization of rays is pivotal to the performance of the system. A primary factor that determines the performance of the fin is phase lags between the rays, which create variations of the effective angle of attack at the leading edge as well as shape changes throughout the fin surface. Structural flexibility of the rays leads to passive deformations of the fin, which can increase the thrust generation and the propulsion efficiency.

Key words: pectoral fin, labriform locomotion, fully coupled simulation.

INTRODUCTION

Fish locomotion is actuated through rhythmic undulation of flexible bodies and/or unsteady flapping of body-attached fins. Morphologically, these fins fall into two categories: median fins (e.g. dorsal fins, ventral fins and caudal fins) and paired fins (e.g. pectoral fins and pelvic fins). Paired fins are employed mostly in motion stabilization, maneuvering and labriform swimming (Webb, 1973; Blake, 1979; Vogel, 1994; Standen, 2008).

In most bony fishes, the attached fins possess a characteristic skeleton-reinforced membrane structure – a soft (and thin) collagenous membrane strengthened by bony fin rays. The Young's modulus of the fin rays is much larger than that of the membrane so that the bending stiffness of the fin is determined mostly by the embedded rays (Lauder et al., 2006; Lauder and Madden, 2007). The non-uniform distribution of these rays imparts anisotropic structural flexibility so that certain deformations may be favored while others are restricted. The basal end of each ray attaches to four separate muscles. This architecture enables a fish to control the motion of each ray individually. In addition, the curvature along a ray can also be actively controlled. According to morphological studies (Harder, 1975; Kardong, 1998), a fin ray contains a central bundle of collagen surrounded by small, segmented bony elements called hemitrichs. These elements are paired and resemble a bimetallic strip with two elongated bony elements separated by the central collagen core. A hemitrich is connected with short ligaments and elastic fibers so that bending moments can be implemented along the length of a ray (Alben et al., 2007).

Recently, ray fins, with their capacity of sophisticated shape control, have attracted much attention owing to their possible applications on bio-inspired engineering. The structural lightness and robustness, controllability, versatility and deployability of these bio-structures make them promising prototypes of novel propulsion systems. Indeed, experimental tests have been undertaken to study hydrodynamic performance of a mechanical replica of a ray fin (Tangorra et al., 2007).

Our study is motivated not only by the scientific need to understand the structure *vs* function of ray fins but also by the biomimetic applications of these bio-structures on autonomous underwater vehicles (AUVs) or micro-aerial vehicles (MAVs). The high efficiency and versatility of this design are especially useful under complex conditions, e.g. in confined space, low speed and unsteady currents. Our primary objective is to identify essential characteristics of ray fins that contribute most to their locomotion performance. From the biomimetic point of view, it is convenient to create simple, easily manufactured devices possessing essential characters of fish fins rather than exact copies of nature. For this reason, instead of exactly duplicating the fin of a specific species (Ramamurti et al., 2002; Mittal et al., 2006), in the current investigation we consider idealized fins with simplified geometry, internal structure and kinematics.

In a previous work we have computationally examined the dynamics of a trapezoid fin supported by a number of nonlinear beams resembling the caudal fins of bony fishes (Zhu and Shoele, 2008). Numerically, the fluid–structure interaction problem was solved by coupling a large Reynolds number boundary-element method (BEM) with a nonlinear Euler–Bernoulli beam model. At the base ends, the orientations of the rays are controlled individually, a pivotal characteristic that allows for different locomotion modes to be achieved through synchronized ray motions. For example, by synchronizing the rays a caudal fin can undergo both homocercal (with dorso–ventral symmetry) and heterocercal (with dorso–ventral asymmetry) motions. In both cases, passive flexibility of the rays greatly increases the propulsion efficiency of the fin. Moreover, it also reduces lateral force generation and the sensitivity of propulsion efficiency to kinematic parameters. Both of these features are beneficial to the performance of the fin.

We herein propose a numerical study of a fin that is geometrically, structurally and kinematically similar to a pectoral fin during labriform swimming [specifically, as discussed later, the parameters chosen in this study are close to data measured from striped surfperch (Drucker and Jensen, 1996a; Drucker and Jensen, 1996b; Drucker and Jensen, 1997)].

At low speed, labriform swimming using pectoral fins is a primary mode of locomotion (Webb, 1973). Two extreme cases of fin movements, drag-based (i.e. rowing) and lift-based (i.e. flapping), have been identified (Blake, 1983; Vogel, 1994), although it is known that pectoral fin motions are usually complicated and rarely exhibit pure drag-based or lift-based movements (Gibb et al., 1994). In drag-based propulsion, it is found that with rigid fins positive thrust is generated in half of the period (i.e. no thrust generation during the recovery phase) so that the duty factor is 50% (Blake, 1981; Lauder and Jayne, 1996). Recently Mittal et al. (Mittal et al., 2006) and Tangorra et al. (Tangorra et al., 2008) have demonstrated that with structural flexibility the duty factor can be increased to 100%. In lift-based propulsion positive thrust generation is obtained during the whole flapping period and the duty factor may approach 100% (Vogel, 1994; Walker and Westneat, 2002). It was also found that lift-based propulsion generated higher efficiency, while drag-based propulsion generated higher thrust. Based upon this, it was suggested that drag-based mode was employed mostly in low speed maneuvering, while lift-based mode was used in power-conserving cruising (Kato, 1999; Archer et al., 1979). Incidentally, the lift-based mode is much simpler kinematically than the drag-based mode and thus easier to materialize in biomimetic devices.

Our focus is upon the performance of a pectoral fin in lift-based thrust generation (Westneat, 1996; Walker and Westneat, 1997). The major aspects we are going to test in this numerical study are: (1) effects of leading edge vortices (LEV) to the propulsion performance of the fin; (2) significance of the synchronization of ray motions; and (3) effects of the structural flexibility of the rays. Towards this end, we apply a fully coupled fluid–structure interaction model in which the rays are modeled as Euler–Bernoulli beams and the fluid motion is solved as potential flow. Vorticity generations from both the trailing edge and the leading edge are modeled as shear layers and mathematically represented as distributions of dipoles on thin sheets.

The paper is organized as follows. We first specify the geometry, internal structure and kinematics of the idealized fin. The fluid–structure interaction model, including the BEM (with LEV incorporated) and the fully nonlinear structural model, is then briefly described. Using this model, we investigate the dynamics and near-body flow field of the flapping fin, focusing on the effects of fin kinematics as well as structural flexibility. Finally, conclusions are drawn.

MATERIALS AND METHODS
Physical model of a paired fin and its kinematics

As shown in Fig. 1, we consider a skeleton-reinforced fin, which is reminiscent of the pectoral fins of a fish (e.g. Drucker and Jensen, 1997; Thorsen and Westneat, 2005). The fin is supported by 15 rays, tagged Ray 1 to Ray 15. A Cartesian coordinate system (x, y, z) is defined, within which the base ends of the rays form a baseline, which lies on the x-axis with length x_0. The trailing ends outline the trailing edge of the fin. The base ends of the rays are pinned during the motion. The fin has a uniform thickness d except for the vicinity of the trailing edge (within a region around 4% of the chord length) where tapering is implemented. The purpose of this tapering on the profile of the fin is to create a sharp trailing edge required
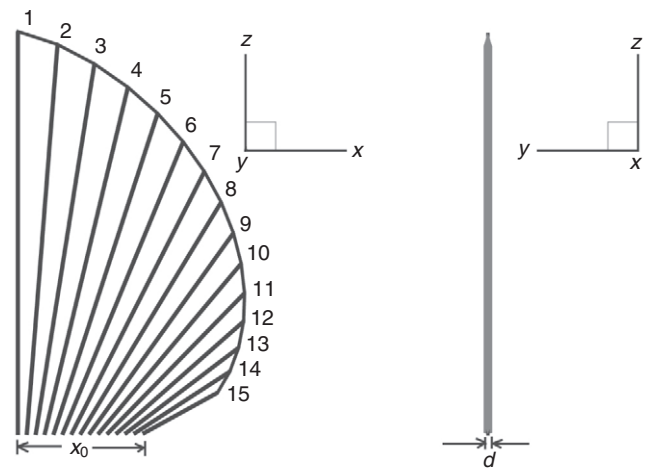

Fig. 1. Geometry and internal structure of the fin. x_0, length of baseline; d, thickness of fin.

for implementation of the Kutta condition as discussed later. It does not affect the rays (i.e. they are still considered to be uniform beams). θ_i, the angle between the base end of Ray i and the x-axis, varies evenly from 90 deg. (Ray 1) to 30 deg. (Ray 15) and does not change with time during the flapping motion. The length of Ray i, L_i, is given as $L_1\{1-0.8[(i-1)/14]^{5/4}\}$, where L_1 is the length of Ray 1 (the ray at the leading edge).

The fin undergoes a translational motion in the x direction with constant speed U. To achieve lift-based thrust generation, a dorso–ventral flapping is activated by rotating each individual ray around the baseline. The angle between Ray i and the x–z plane is denoted as α_i and prescribed as $\alpha_i=\alpha_0[1-\cos(\omega t-\varphi_i)]/2$, where ω is frequency, φ_i is the phase of the i-th ray in rolling and t is time. According to this depiction, during the flapping motion each ray rotates (with the baseline as the rotating axis) between $\alpha_i=0$ and α_0 (α_0 is maximum angle of rolling of each ray in one stroke). During the downstroke period a ray goes from $\alpha_1=0$ to α_0. The recovery from α_0 to 0 occurs in the upstroke period.
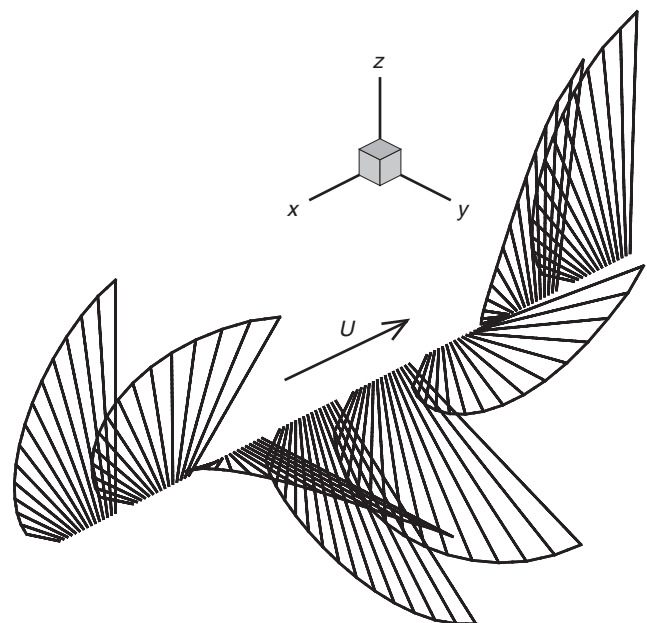

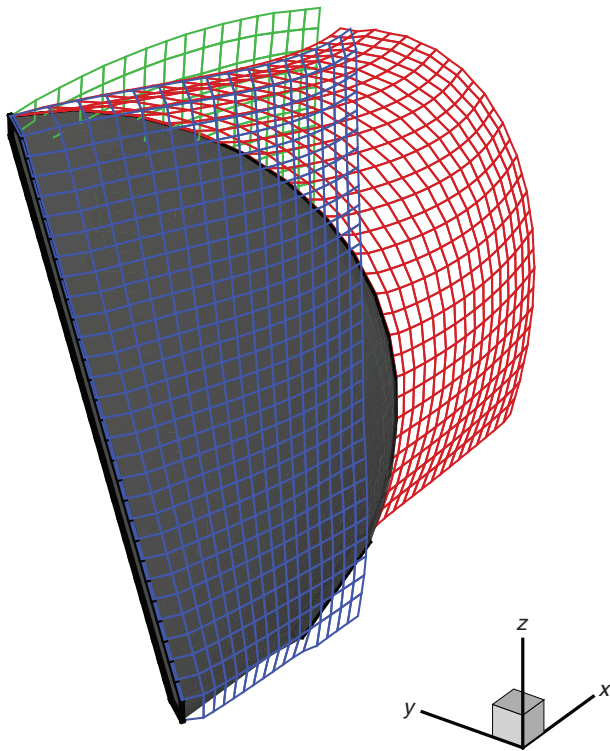Fig. 2. Kinematics of fin flapping with φ_{15}=45 deg. U, forward speed.

position (α_i=0). Thus, in our simulations we consider only one period of flapping motion. The motion starts from the vertical position (Fig. 2). It is then followed by a downstroke and an upstroke (also known as abduction and adduction, respectively). The motion starts from Ray 1 and ends at the moment it returns to its original position (i.e. the duration of simulation is $T=2\pi/\omega$). Unless otherwise specified, for simplicity we assume that the phase φ_i varies linearly from φ_1=0 to φ_{15}; thus, φ_{15} is used as a metric of the phase difference between neighboring rays. Both the structural deformation of the rays and the phase difference between them can cause the bow shape in lateral view as observed in experiments (Drucker and Jensen, 1997).

In the following calculations, we use L_1=0.1 m, x_0=0.03 m, d=2 mm, α_0=145 deg. and U=0.5 m s^{-1}. Although we aim at examining the mechanical principles about this type of design in general rather than the performance of a particular species, the choice of these parameters has certain biological relevance. Specifically, most parameters in this study are chosen following the experimental measurements by Drucker and Jensen of striped surfperch (*Embiotoca lateralis*) (Drucker and Jensen, 1996a; Drucker and Jensen, 1996b). In high-speed labriform cruising, this fish achieves a speed of 0.48 m s^{-1}, around 80% of pectoral caudal gait transition speed. As shown in their experiments, the flapping amplitude of the fin tip is about twice the span of the fin, and the Strouhal number based upon the flapping period reported by Drucker and Jensen (Drucker and Jensen, 1997) is around 0.3–0.4. These are within the range of the fin kinematics considered in our present study.

Structural dynamics model

Despite the fact that rays have complicated internal structures and are usually tapered/branched near the trailing ends, for simplicity in our model the rays are depicted as cylindrical Euler–Bernoulli beams with uniform cross-sections. These beams can be stretched (with tensile stiffness EA, where E is the Young's modulus and A is the cross-sectional area) or bent (with bending stiffness EI). In this study we concentrate on the passive deformability of the rays,
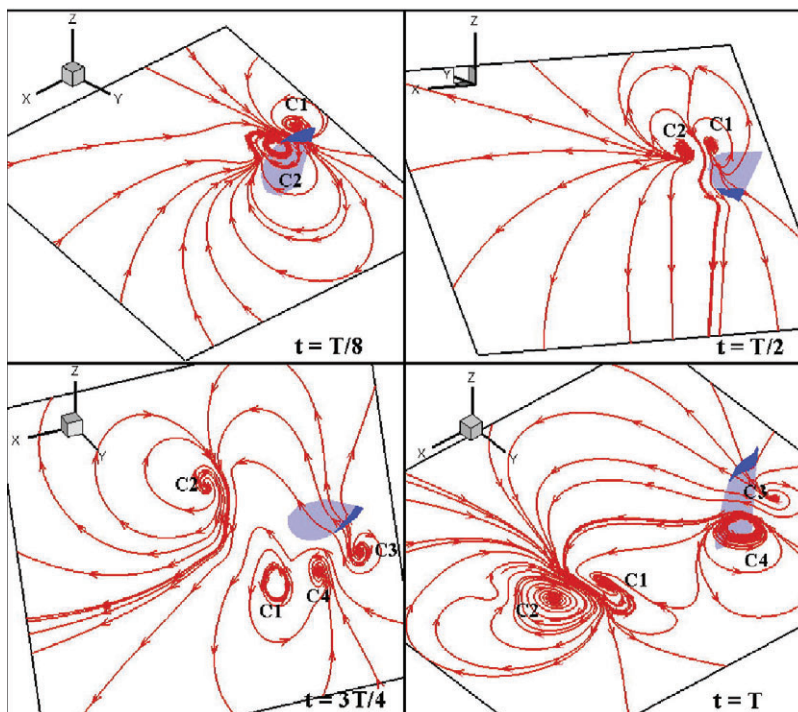

Fig. 3. Vorticity sheets shed from the trailing edge (in red) and the leading edge (in blue and green).

We also define a Strouhal number $S_t \equiv \omega L_1/2\pi U$, where U is the forward speed. In this study we focus on a range of S_t between 0.1 and 0.5. To imitate observed fin activation at moderate swimming speed (Gibb et al., 1994), we assume that between fin strokes there are periods of inactivity during which the fin is held in its vertical

Fig. 4. Streamlines within a plane rotating with Ray 1 (the leading edge) during a flapping period. Strouhal number S_t=0.4, φ_{15}=60 deg. Leading edge vortex (LEV) is included and the rays are flexible. t, time; T, period. C1, C2, C3 and C4 are regions of circulation.
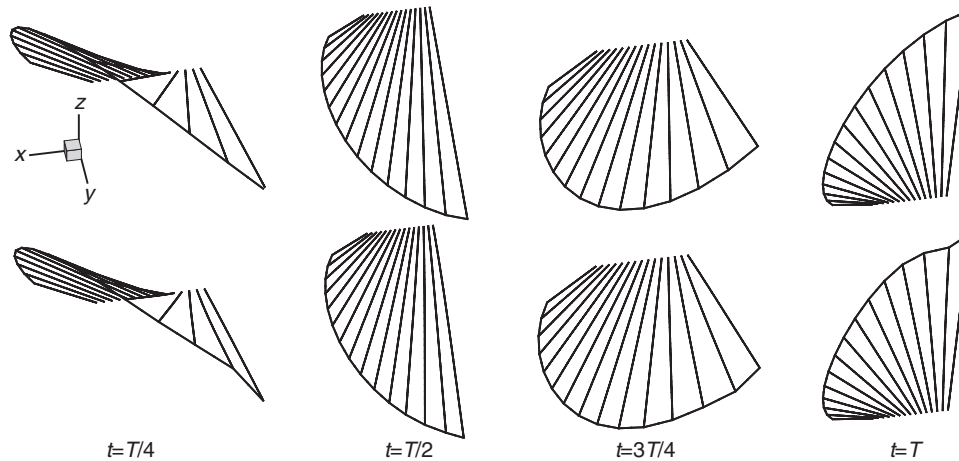
Fig. 5. Deformation of the fin during one flapping period with rigid (upper row) and flexible (lower row) rays. Strouhal number $S_t=0.4$, $\varphi_{15}=60$ deg. Leading edge vortex (LEV) is included. t, time; T, period.

while the active deformability activated by the muscles/tendons connected to the rays (Alben et al., 2007) is not considered.

Numerically, a three-dimensional nonlinear model is employed to simulate the dynamics of the rays (Zhu and Shoele, 2008). This method was originally developed to study the fully nonlinear dynamics of marine cables (Tjavaras et al., 1998), and is characterized by its capacity to simulate arbitrary configurations and large deformations owing to the implementation of a dual Euler–Lagrangian coordinate system and the robust Euler parameters (e.g. Junkins and Turner, 1986) instead of the more conventional Euler angles, which suffer from singularities.

To elaborate, by invoking the conservation of momentum we have (Tjavars, 1996):

$$m\left(\frac{\partial \mathbf{V}}{\partial t}+\boldsymbol{\omega}\mathbf{V}\right)=\frac{\partial \mathbf{T}}{\partial s}+\boldsymbol{\Omega}\mathbf{T}+\left(1+\varepsilon\right)\left(\mathbf{F}_h+\mathbf{F}_c\right)\,, \qquad (1)$$

where m is the mass per unit length, s is a Lagrangian marker measuring the distance from a point on the ray to the basal end along the unstretched ray, ε is the strain, $\mathbf{V}$ and $\boldsymbol{\omega}$ are the translational and angular velocities, respectively, $\mathbf{T}$ is the internal force inside the ray, $\mathbf{F}_c$ is the constraining force from the membrane that controls the distance between neighboring rays and $\mathbf{F}_h$ is the hydrodynamic force on each ray.

Similarly, from conservation of angular momentum another set of equations is obtained as:

$$\frac{\partial \mathbf{M}}{\partial s}+\boldsymbol{\Omega}\mathbf{M}+\left(1+\varepsilon\right)^3\boldsymbol{\tau}\mathbf{T}=0\,, \qquad (2)$$

where $\mathbf{M}$ is the internal moment. $\boldsymbol{\Omega}$ is the Darboux vector measuring the material torsion and curvatures of the ray. $\boldsymbol{\tau}$ is the tangential vector along the ray. $\mathbf{M}$ and $\boldsymbol{\Omega}$ are related by $M_\tau=GJ\Omega_\tau$, $M_n=EI\Omega_n$ and $M_b=EI\Omega_b$. The subscripts τ, n and b represent components in the tangential, normal and bi-normal directions, respectively, and GJ represents the torsional stiffness. In the following simulations with flexible rays, unless otherwise specified we assume $E=1$ GPa (e.g. Lauder et al., 2006); a much larger E (100 GPa) is applied to approximate the behavior of a rigid ray. Because no twisting motion is considered, the value of GJ is irrelevant. To model the viscoelastic behavior of the rays, we further replace E by $E+D\partial/\partial t$, where the viscous coefficient D is chosen to be 0.4 sGPa. The diameters of
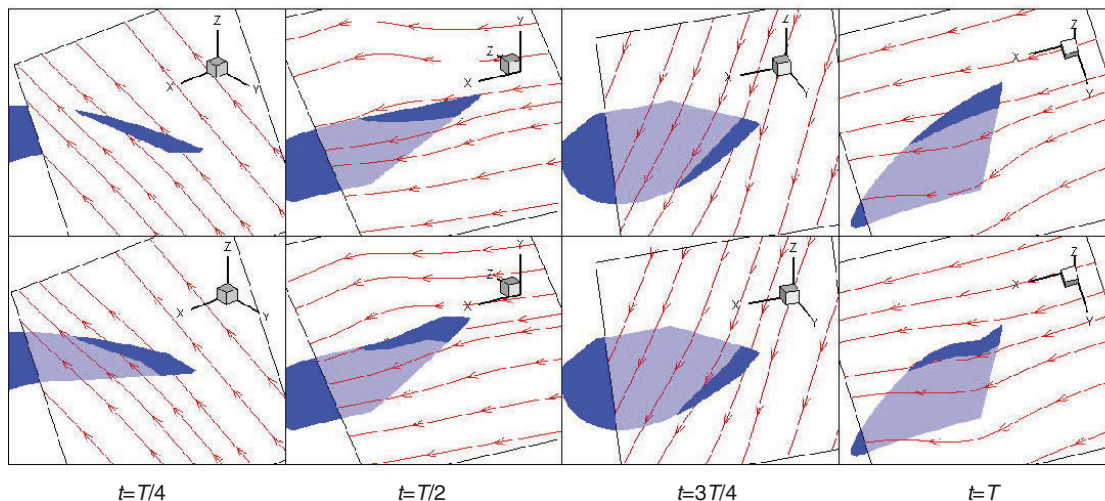

Fig. 6. The flow field (streamlines) within the same rotating plane as in Fig. 4 viewed from a coordinate system moving with the point where the leading edge intersects this plane. Strouhal number $S_t=0.4$, $\varphi_{15}=60$ deg. Leading edge vortex (LEV) is included and the rays are flexible. t, time; T, period.
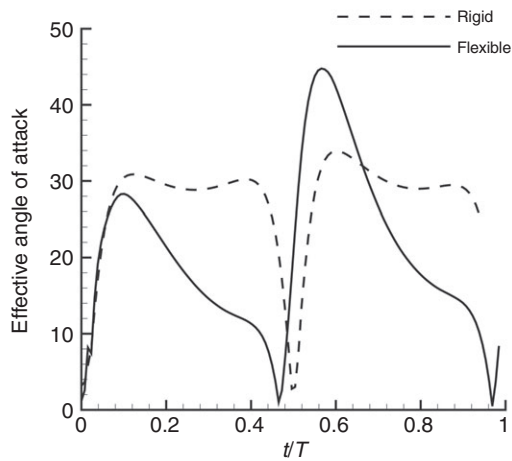
Fig. 7. Comparison of the effective angles of attack near the tip of the leading edge between a fin with rigid rays and one with flexible rays. Leading edge vortex (LEV) is included. t, time; T, period.

the rays are estimated by using the argument in Alben et al. (Alben et al., 2007), i.e. during normal swimming the bending energy stored in the fin must be balanced by the kinetic energy of the flow. According to their estimation, for this to be true the EI of a ray, its length L and the swimming speed U must be related by $EI/L < U^2 L^3/12$, based upon which we choose the radius of a ray to be 1 mm.

For the i-th ray, its base end is pinned in space with the orientation determined by the angles θ_i and α_i. Its trailing end is treated as a free end with no external load. The resulting system of nonlinear equations is solved by an efficient finite difference algorithm, the modified box method (Tjavaras, 1996).

The hydrodynamic load on the rays is imposed *via* the attached membrane, which is modeled as arrays of linear springs connecting the neighboring rays. According to Lauder et al. (Lauder et al., 2006), the membrane between fin rays has a modulus of about 0.3–1.0 MPa. If its thickness is smaller but comparable with the effective diameter of the ray, the spring constant per unit length should be $O(10^3)\,\mathrm{N\,m}^{-2}$;

in this study we choose the spring constant to be $2000\,\mathrm{N\,m}^{-2}$. The rays are assumed to have the same density as water. The mass of the membrane is not considered because it is much smaller than the added mass.

Fluid dynamics model

We consider cases with large Reynolds numbers (Re) so that the flow field can be described by defining a flow potential $\Phi(\mathbf{x},t)$, where $\mathbf{x}=(x, y, z)$ is the position vector [as demonstrated by Anderson et al. (Anderson et al., 1998)], predictions from a potential flow model are in reasonable agreement with experimental measurements for a flapping foil when $Re\sim O(10^4)$. The vorticity shed from the trailing edge of the fin is physically modeled as a zero-thickness shear layer and mathematically represented by a thin sheet of distributed dipoles. The strength of the newly shed vortices is determined by the Kutta condition at the trailing edge (Zhu et al., 2002).

A key characteristic of our current fluid dynamics model is the inclusion of vorticity shed from the leading edge area. Following the treatment of leading edge separations within the potential flow framework (Katz, 1980; Dong, 2007), we model the leading edge separation as thin shear layers (i.e. in the same fashion as the trailing edge separation). This depiction, *per se*, is consistent with experimental visualizations that show that vorticity shed from the leading edge area starts as thin vorticity layers before they roll-up and form individual vortices (Taneda, 1977).

Katz studied the dynamics of two-dimensional flow around a thin plate (Katz, 1980). In that model, LEV was depicted as a shear layer initiated from a prescribed separation point near the leading edge. Good comparisons with experiments were achieved over a large range of angle of attack. A similar model was applied to solve the flow around a thin plate, in which vorticity shed from both edges are represented as vortex sheets emanating from the sharp edges (Jones, 2003). Dong extended this method to three dimensions, unsteady flow and finite foil thickness (Dong, 2007). An algorithm was developed to predict the unsteady separation lines by using the adverse pressure gradient (Faltinsen and Pettersen, 1987). The accuracy of this method has been tested *via* comparisons with experimental measurements of a foil undergoing pitching and heaving motions (Read, 2000). It was demonstrated that by including
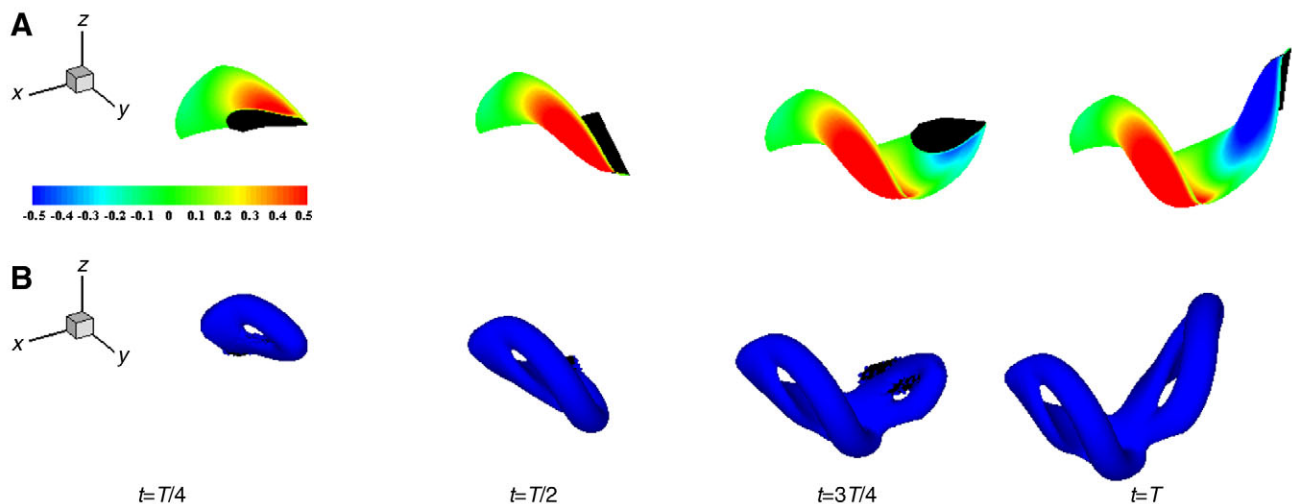

Fig. 8. (A) Strength of dipole distribution in the vorticity layer shed from the trailing edge (normalized by UL_1). (B) Iso-surface of the vorticity field. Leading edge vortex (LEV) is not included in this simulation. Strouhal number $S_t=0.4$, $\varphi_{15}=60$ deg. The rays are flexible. t, time; T, period, U, forward speed; L_1, length of Ray 1.
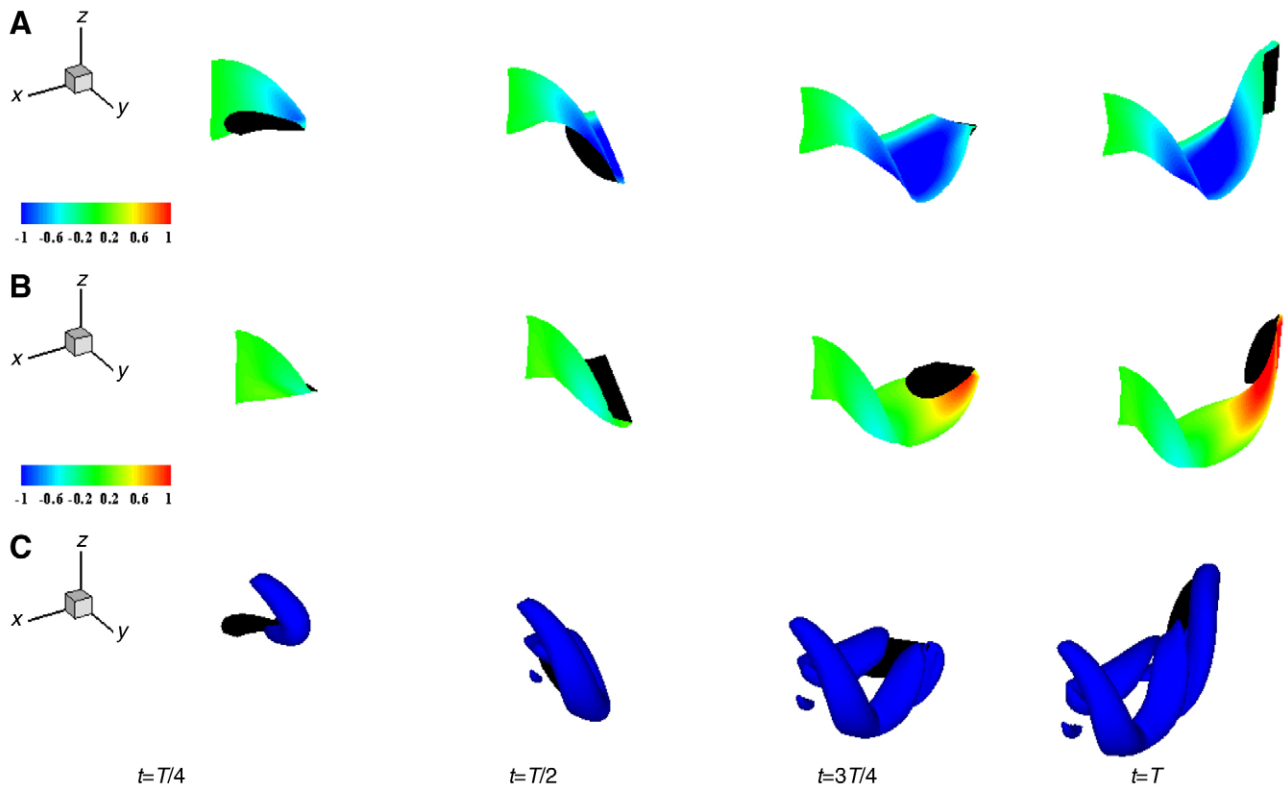
Fig. 9. Strength of dipole distribution of the vorticity layer shed from (A) the upper side of the leading edge, and (B) the lower side of the leading edge. The dipole strength is normalized by UL_1 (C) Iso-surface of the vorticity field generated by the leading edge vortices (LEV). Strouhal number S_t=0.4, φ_{15}=60 deg. The rays are flexible. t, time; T, period, U, forward speed; L_1, length of Ray 1.

this simplified LEV representation the accuracy of the potential flow based prediction is significantly improved. Specifically, it was found that in general the incorporation of LEVs greatly reduce the predicted thrust generation.

Taking advantage of the special geometry of the fin we study, in our model we assume that the locations of leading edge separation are fixed at sharp edges existing near the leading edge, so that although we model LEV in the same manner as the abovementioned studies, the complicated algorithm to locate separation lines is not required. Furthermore, by using two vortex sheets shed alternatively, one from the upper side and the other from the lower side of the leading edge, we assume that each vortex sheet remains on its side of the fin, so that the singularity associated with a vortex sheet passing through the fin is avoided. Otherwise to eliminate this singularity it requests special treatment (Dong, 2007).

As shown in Fig. 3, in our approach the LEV is modeled as two shear layers, one from the upper side and the other from the lower side of the leading edge, where sharp angles exist between neighboring panels. Similar to their trailing edge counterpart, the strengths of these shear layers are determined by invoking the Kutta condition. In addition, to prevent interceptions of these shear layers with the fin itself, which will induce singularity, at each time step the distances between the shear layers and the fin are carefully monitored. Whenever interception is likely to occur, the shear layer is pushed away from the fin so that singularity is prevented. Although our model allows continuous vorticity generation from both separation lines at the leading edge, it has been demonstrated in our results that at any given moment only one of them is associated with significant vorticity shedding.

Fluid–structure coupling

To solve the fluid and the structural problems simultaneously in a fully coupled algorithm, we employ the following iteration method: at each time step to start the iteration we apply an initial guess of fin deformation and solve the hydrodynamic problem through the BEM. Based upon this the hydrodynamic load is updated and applied to calculate the body deformation; if this recalculated deformation is not sufficiently close to the initial guess it is used as the initial guess in the next iteration step.

Detailed description and validation of this iteration method are provided in previous publications (Zhu, 2007; Zhu and Shoele, 2008).

Numerical issues

Numerically, the fluid dynamics problem is solved using a boundary-element approach by discretizing the fin surface S_b into N_b panels S_{bj}, j=1, ..., N_b, and the wake surfaces S_w into N_w panels, where N_b is the total number of panels on the fin surface, S_{bj} represents one panel and N_w is the number of panels on the wake. By satisfying the no flux condition at the centroids of the panels on the fin surface this boundary value problem is formulated as a system of linear equations and solved numerically (Katz and Plotkin, 1991; Zhu et al., 2002).

After obtaining $\Phi(\mathbf{x},t)$, the hydrodynamic pressure (p) is determined through Bernoulli's equation, and given as:

$$p(\mathbf{x},t) = -\rho \left\{ \frac{\partial \Phi(\mathbf{x},t)}{\partial t} + \frac{1}{2} \left| \nabla \Phi(\mathbf{x},t) \right|^2 \right\}, \qquad (3)$$
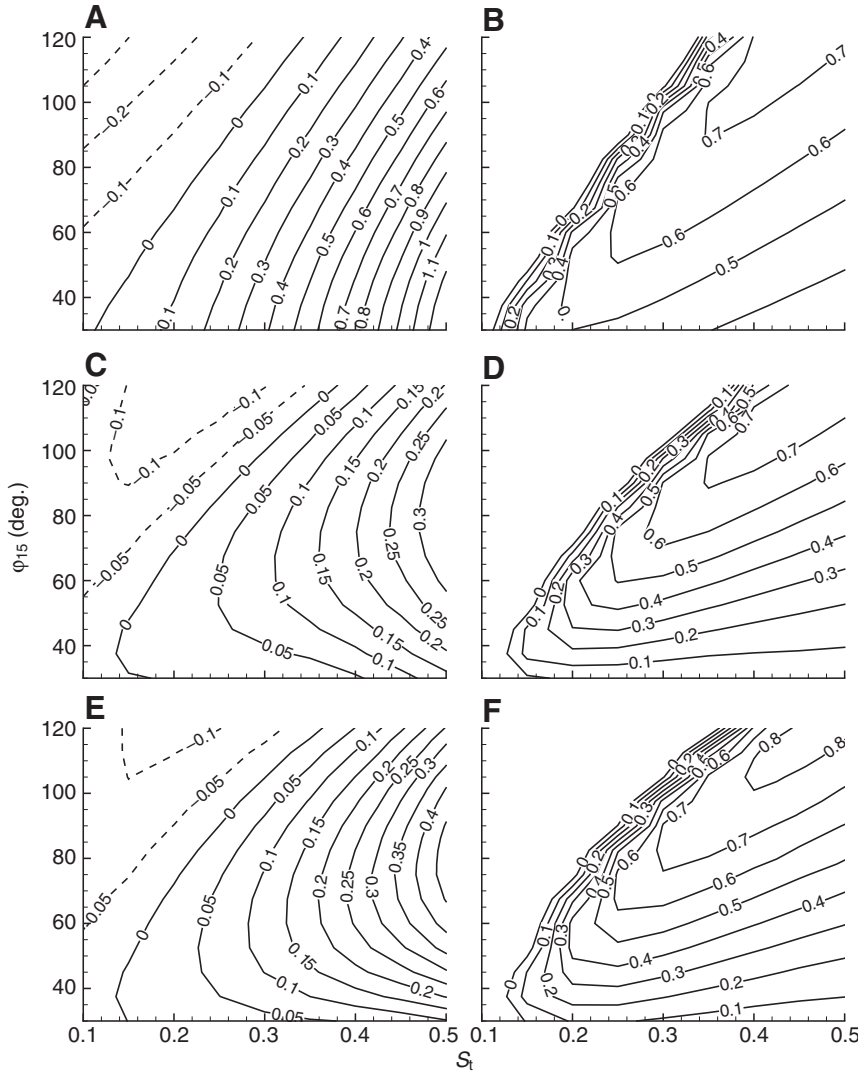
Fig. 10. (A) Mean thrust coefficient $\bar{C}_T$ and (B) propulsion efficiency η as functions of the Strouhal number S_t and the phase lag φ_{15} without considering the effect of leading edge vortices (LEV) (the rays are rigid). (C) $\bar{C}_T$ and (D) η as functions of S_t and φ_{15} when LEV is included in the simulation (the rays are rigid). (E) $\bar{C}_T$ and (F) η as functions of S_t and φ_{15} when LEV is included in the simulation and the rays are flexible. Negative values of the C_T are shown in broken lines.

where ρ is the density of water ($10^3\,\mathrm{kg\,m^{-3}}$). We assume that the hydrodynamic force acting on this panel, $p\Delta S_{bj}$ (ΔS_{bj} is the area of the panel), is transferred equally to four grid points that are closest to the panel on the two neighboring rays (two points on each ray).

Hydrodynamic forces

Integrating p over the fin surface, we obtain the overall hydrodynamic force on the fin (**F**) as:

$$\mathbf{F} = \iint_{S_b} p(\mathbf{x}',t)\mathbf{n}\,d\mathbf{x}', \qquad (4)$$

where **n** is a unit normal vector pointing into the fin. The power (P) required to drive the fin is given as:

$$P = \iint_{S_b} p(\mathbf{x}',t)\mathbf{n}\cdot\mathbf{V}_b(\mathbf{x}',t)\,d\mathbf{x}', \qquad (5)$$

where $\mathbf{V}_b$ is the instantaneous velocity at the surface of the fin.

The propulsion efficiency η is defined as:

$$\eta = \bar{F}_T U / \bar{P}, \qquad (6)$$

where $\bar{F}_T = -\bar{F}_x$ and $\bar{P}$ represent the thrust force and power consumption averaged over one period T, respectively. To characterize the hydrodynamic performance of the fin, we herein define a mean thrust coefficient $\bar{C}_T = \bar{F}_T / \frac{1}{2}\rho L_1^2 U^2$.

The dynamics of the fin is also characterized by generation of lift force F_z and lateral force F_y. Correspondingly, we will examine the lift coefficient $C_L = F_z/\frac{1}{2}\rho L_1^2 U^2$ and the lateral force coefficient $C_y = F_y/\frac{1}{2}\rho L_1^2 U^2$, focusing upon the first-harmonic components $C_L^{(1)} = 2/TRe\{\int_0^T C_L(t)e^{i\omega t}dt\}$ and $C_y^{(1)} = 2/TRe\{\int_0^T C_y(t)e^{i\omega t}dt\}$.

RESULTS

Using the fully coupled model we study cases with $S_t = 0.1\sim 0.5$ and φ_{15} varying from 30 deg. ($\pi/6$) to 120 deg. ($2\pi/3$). To put this choice of phase lag in perspective, we note that, according to Webb (Webb, 1973), the phase lag between leading and trailing edges varies with swimming speed, ranging from π at $0.2\,BL\,\mathrm{s^{-1}}$ to 0.2π at higher velocities.

Flow visualization and fin deformation

We first study the near-body flow field around the fin as well as the deformation of the fin itself during a single downstroke–upstroke period.

In Fig. 4 we plot the in-plane streamlines within a plane parallel to the rotating axis (i.e. the baseline). This plane rotates with Ray 1 and its distance to the baseline remains as $0.75L_1$. The fin is flexible with $S_t = 0.40$ and $\varphi_{15} = 60$ deg. Four snapshots at different phases of motion are shown. At $t = T/8$ (i.e. at the beginning of the downstroke

motion), a pair of counter-rotating circulations are generated, one from the leading edge (marked as C1) and the other from the trailing edge (marked as C2). These circulations are then shed into the wake (see the snapshot at $t=T/2$). After the transition from downstroke to upstroke motions, a new pair of circulations (C3 and C4) appears ($t=3T/4$). Thus, at the end of the upstroke period ($t=T$), two pairs of vortices are left in the wake. This sequence of vortex shedding is qualitatively consistent with the depiction by Lauder and Drucker (Lauder and Drucker, 2004).

Fig. 5 displays structural deformations of the fin during a flapping period. For comparison, in the same figure we also draw the shapes of a fin with rigid rays. It is seen that effects of ray flexibility is most pronounced near the leading edge. This is attributed to the several facts. First, the rays in that vicinity are longer and thus more deformable than others. Second, the ray at the leading edge (Ray 1) is loaded from one side only so that its deformation is different from neighboring rays, which sustain hydrodynamic loads from both sides.

The deformability of the rays has profound effects upon the interaction between the fin and the surrounding flow field. Our simulations demonstrate that it may significantly change the effective angle of attack at the leading edge. For example, in Fig. 6 we plot the in-plane streamlines of the flow field measured in a reference system fixed on the leading edge of the fin (i.e. this reference system follows both the forward and the lateral motions of the intersection point between this plane and the leading edge). During most of the cycle (except for the snapshot at $t=T/2$, when the transition from downstroke to upstroke occurs), the leading edge of the flexible fin is better aligned with the incoming flow than that of the rigid fin. This effect is more clearly shown by plotting the magnitude of the effective angle of attack at the tip of the fin (i.e. the angle between the leading edge and the incoming flow vector measured in the moving coordinate system) (Fig. 7). As illustrated in previous experiments using flapping foils (e.g. Anderson et al., 1998), such a reduction in effective angle of attack may mitigate generation of LEV.

Fig. 8 shows the three-dimensional flow field visualized *via* dipole distribution within the vorticity layer as well as iso-surfaces of vorticity behind a fin when only the TEV are accounted. It is seen that concentrations of dipoles, displayed in Fig. 8A as red and blue areas, correspond to three-dimensional vortex rings in Fig. 8B. Within one flapping period, two connected vortex rings, one during upstroke and the other during downstroke, are generated, forming a figure of '8' shape in the wake. As shown in Fig. 9A,B, with LEV included during the downstroke period the LEV is generated primarily at the upper side, while in the upstroke period the vorticity sheds from the lower side. In Fig. 9C we plot the iso-surfaces of the vorticity field created by the LEV only (i.e. influences of the TEV and the body itself are not considered). Owing to the complexity of the vorticity field, it is difficult to observe clearly defined vortex rings in the wake.

To summarize, during the downstroke motion two concentrations of vorticity, one from the trailing edge of the fin and the other from the upper side of the leading edge, are generated and shed into the wake. Two additional vorticity concentrations are shed during the upstroke period from the trailing edge and the down side of the leading edge, respectively.

Thrust generation and propulsion efficiency of the fin

In Fig. 10A,B we plot the mean C_T and the η (defined as $U \times$ the mean thrust divided by the mean power expenditure) as functions of the S_t and φ_{15}, the phase lag of Ray 15 (the phase φ_i varies linearly from 0 when $i=1$ to φ_{15} when $i=15$). No LEV is included in the
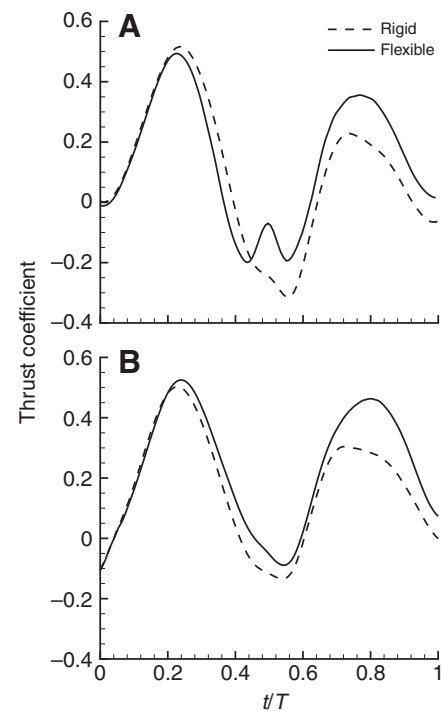

Fig. 11. Variation of the thrust coefficient C_T over one period with (A) φ_{15}=40 deg. and (B) φ_{15}=60 deg. Strouhal number S_t=0.4. Fins with both flexible and rigid rays are considered. t, time; T, period.
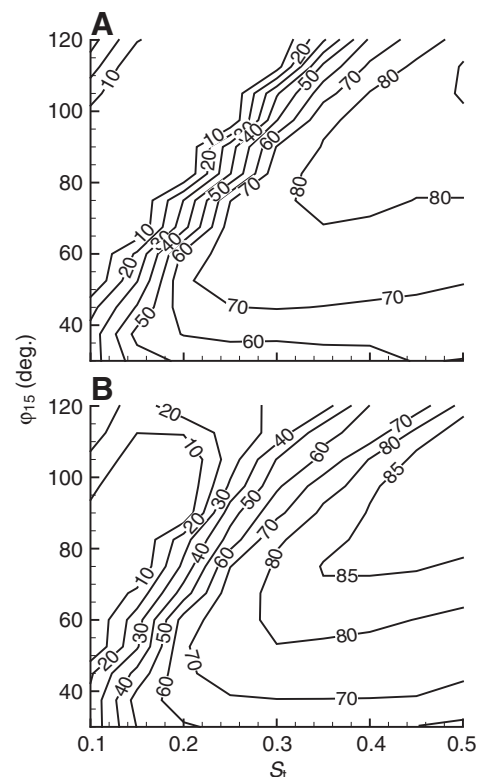

Fig. 12. Duty factor (in percentage) as a function of Strouhal number S_t and φ_{15} with (A) rigid rays and (B) flexible rays.
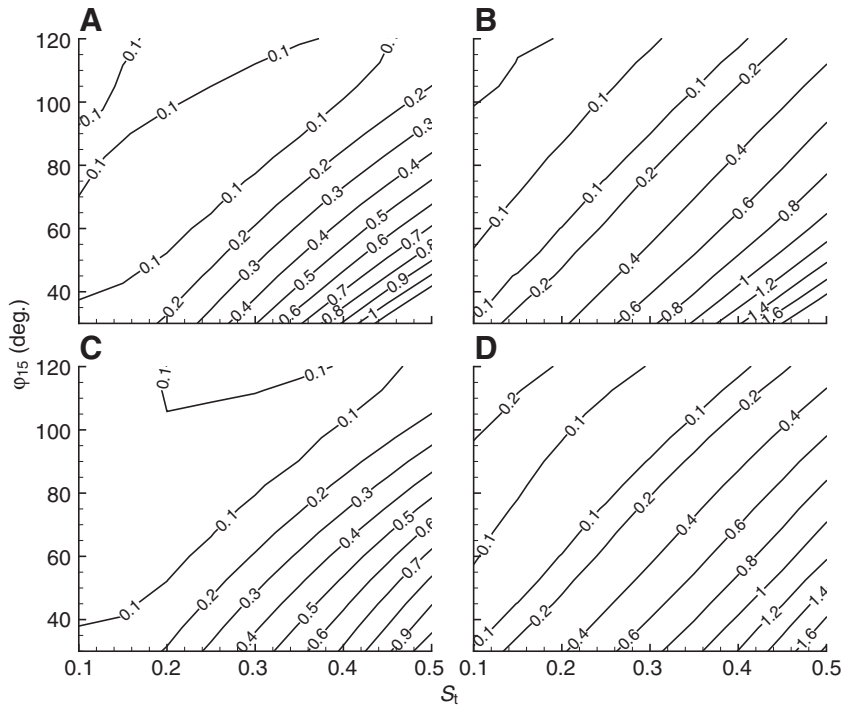
Fig. 13. First-harmonic lateral (A) and lift (B) force coefficients as functions of Strouhal number S_t and φ_{15} for a rigid fin. First-harmonic lateral (C) and lift (D) force coefficients as functions of S_t and φ_{15} for a flexible fin.

simulation and the rays are assumed to be rigid. As shown in the figures, for fixed φ_{15}, C_T increases with S_t, while η reaches its maximum value at an optimal S_t, which depends upon φ_{15}. However, when S_t is fixed, positive thrust and η are achieved only when φ_{15} is below a threshold value, which increases with S_t.

The inclusion of LEV (even though the rays are still rigid) significantly changes C_T (Fig. 10C) as well as η (Fig. 10D). Most notably, the mean thrust is greatly reduced. Within the range of parameters considered in this study (i.e. $0.1 < S_t < 0.5$, 30 deg. $< \varphi_{15} < 120$ deg.), as predicted by the model without LEV the maximum C_T is around 1.3 whereas with LEV this value is merely 0.35. In both cases, however, predictions of the maximum values of η are around 0.75. The effect of LEV is most pronounced in small values of φ_{15}. Our simulations show that, with LEV included,

Fig. 14. The mean thrust coefficient $\bar{C}_T$ and propulsion efficiency η as functions of the Young's modulus E of the rays. $D = E\,0.4$ s. Strouhal number $S_t = 0.4$, $\varphi_{15} = 60$ deg. D, material damping coefficient of the rays.

positive thrust and efficiency can be obtained only when φ_{15} is sufficiently large ($\varphi_{15} > {\sim}30$ deg.). Large values of φ_{15} also cause negative thrust. Indeed, large φ_{15} corresponds to significant pitching of the fin, which may be applied as a braking mechanism (Drucker and Lauder, 2003). Besides, at large φ_{15} when the thrust generation is close to zero, the discrepancy between predictions with and without LEV becomes insignificant. This is attributed to the fact that in these cases the fin motion resembles the feathering behavior so that the effective angle of attack at the leading edge is minimized and LEV is thus mitigated.

Hereafter, we include LEV in all the testing cases.

The effects of fin flexibility upon thrust generation and η are displayed in Fig. 10E,F. By comparing the mean C_T and the η in flexible cases with rigid cases, it is seen that flexibility has limited effect in low S_t. However, in higher S_t it is able to improve the performance of the flapping fin. To elaborate, the three-dimensional anisotropic flexibility imparted by flexible rays can significantly increase the mean C_T (by 40% in some cases), accompanied by a slight increase in η (by about 10%).

Fig. 11A shows the time history of the C_T over one flapping period at $S_t = 0.4$ and $\varphi_{15} = 40$ deg. It is seen that although the thrust force remains positive over most of the period, there exists a short time interval with negative thrust during the transition between the downstroke and the upstroke motions so that the corresponding duty factor is clearly less than 100%. This is qualitatively consistent with the experimental study of the lift-based swimmer bird wrasse (*Gomphosus varius*) as reported by Walker and Westneat (Walker and Westneat, 2002). Employing the experimentally recorded fin kinematics of this fish (Walker and Westneat, 1997), Ramamurti et al. (Ramamurti et al., 2002) has carried out fully-viscous simulations using an unstructured finite-element method, yielding a time history of thrust similar to our prediction (see fig. 6 in that report). Based upon descriptions in their studies, we estimate that the fin size is around 2.5–3 cm so that peak values of the C_T obtained in their simulations are around 0.5–0.7, which are also comparable with our results. In Fig. 11B we study a case with $\varphi_{15} = 60$ deg. and find that
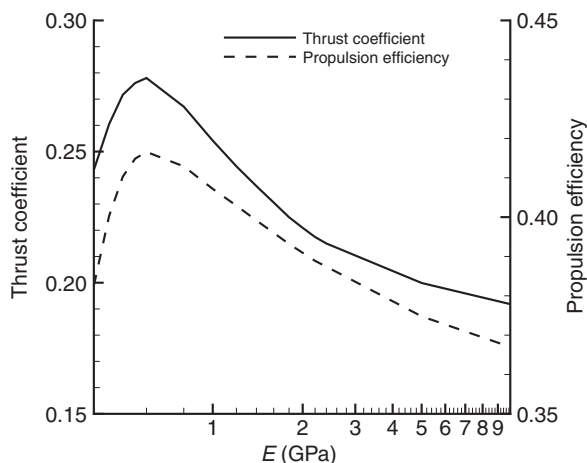
the period with negative thrust is greatly reduced. In both cases (φ_{15}=40 deg. and φ_{15}=60 deg.), the structural flexibility increases the thrust and its effect is most pronounced during the upstroke period, which is consistent with the fin deformation as shown in Fig. 5.

As suggested in Fig. 11, the duty factor clearly depends upon the kinematic parameters as well as the fin flexibility. To further illustrate this, in Fig. 12 we plot the duty factor as a function of S_t and φ_{15}. The effect of flexibility to increase the duty factor is herein quantitatively confirmed. Within this range of parameters, our simulations record a maximum duty factor of 87%.

In Fig. 13 we plot the first-harmonic components of the lift coefficient and the lateral force coefficient as functions of the S_t and the phase lag φ_{15}. Similar to the case in thrusts generation, the influence of structural flexibility is also more pronounced in high S_t. Its specific effect depends upon the range of kinematic parameters under consideration. For example, at S_t=0.4 this flexibility decreases

the lateral force when φ_{15}<45 deg. and increases it otherwise; the lift force is increased when 45 deg.<φ_{15}<105 deg.

We finally check the effect of different levels of ray flexibility, achieved by varying E while keeping the ratio D/E and other parameters unchanged. As shown in Fig. 14, peaks of both C_T and η occur when E is around 0.6 GPa. For sufficiently soft fins significant drop of thrust generation is observed, echoing findings from flexible foils (e.g. Katz and Weihs, 1978; Zhu, 2007).

DISCUSSION

By using a fully coupled model, we have numerically investigated the fluid–structure interaction mechanisms involved in the lift-based propulsion of an idealized pectoral fin. The fin is strengthened from inside by a skeleton of fin rays, which are modeled as Euler–Bernoulli beams. The fin motion is activated by rotations of each individual ray. A 'wing-like' dorso–ventral motion
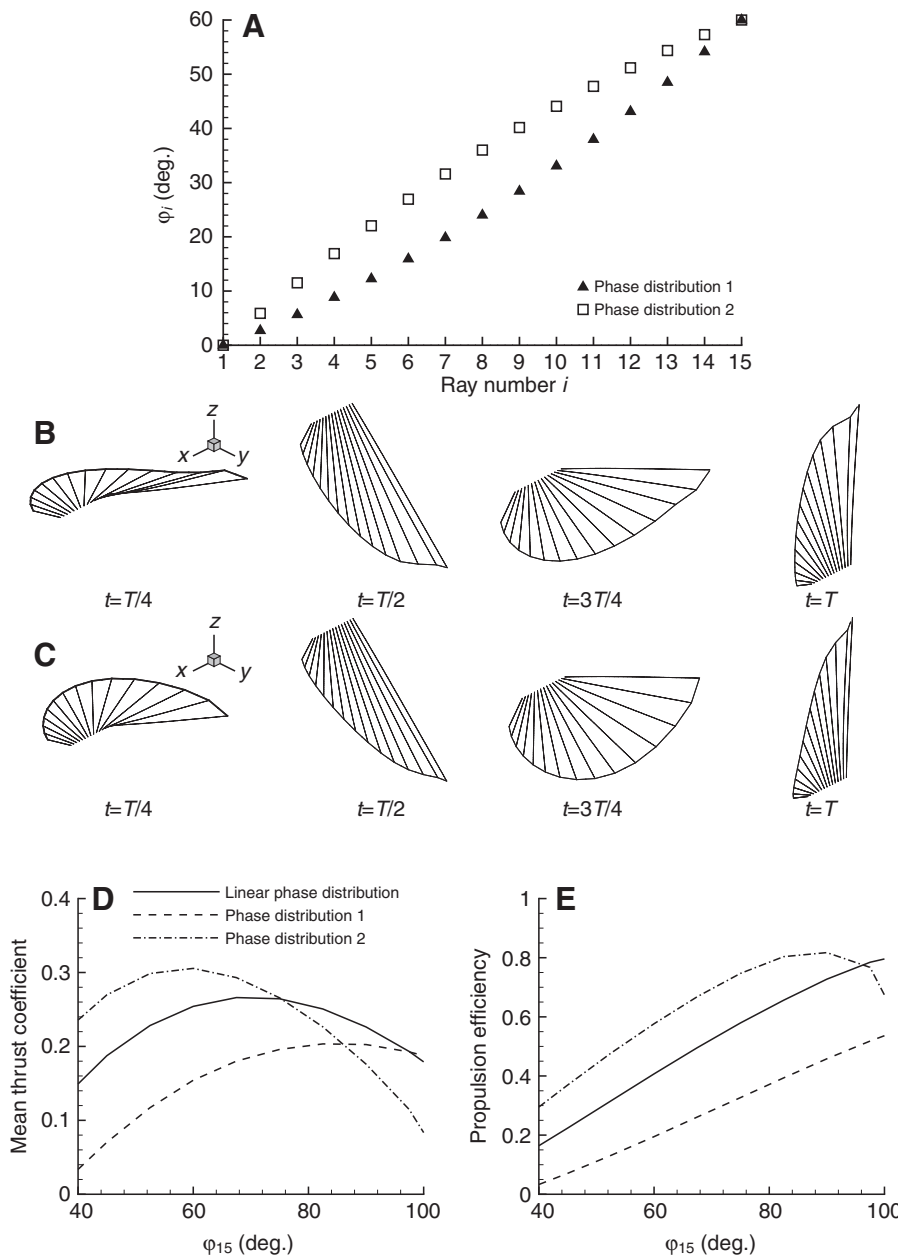
Fig. 15. (A) Phase distribution 1 with $\varphi_i=\varphi_{15}[i-1/14-0.1+0.4(i-1/14-0.5)^2]$ and phase distribution 2 with $\varphi_i=\varphi_{15}[i-1/14+0.1-0.4(i-1/14-0.5)^2]$ (φ_{15}=60 deg.). (B) Fin motion during one period with phase distribution 1. (C) Fin motion during one period with phase distribution 2. In B and C Strouhal number S_t=0.4, φ_{15}=60 deg. (D) Mean thrust coefficient and (C) propulsion efficiency as functions of φ_{15} for phase distributions 1 and 2 as compared with the case with linear phase distribution when S_t=0.4. t, time; T, period; φ_i, phase of the i-th ray in rolling.

characteristic of the lift-based mechanism is achieved by synchronized ray motions.

Our results indicate that the hydrodynamic performance of such a system is determined by its frequency of motion (represented by the Strouhal number), phase difference among the rays, as well as structural properties of the rays. By varying the phases of the rays, the fin achieves a combination of roll and pitch motions. Based on this mechanism the effective angle of attack at the leading edge as well as the shape of the fin can be adjusted so that the thrust generation and the propulsion efficiency can be optimized. With properly chosen kinematic parameters, positive thrust is observed in most of the downstroke–upstroke period. High propulsion efficiency (with a peak value of ~0.8 within the range of parameters considered in this study) is observed.

We studied the effect of passive deformation of the fin due to structural flexibility of the rays. Our results show that such passive deformations indeed increase the thrust generation as well as the propulsion efficiency [although the increase in efficiency is not as significant as in the case of caudal fins (Zhu and Shoele, 2008)]. By visualizing the near-body flow field we find that a primary effect of structural flexibility is the reduction of the effective angle of attack, which suggests a mechanism for the change in performance.

Further investigation shows that performance of the system depends not only upon φ_{15}, the maximum phase lag between all the rays, but also upon the detailed distribution of the phases. For example, in Fig. 15 we plot the thrust coefficient and propulsion efficiency of the fin when φ_i are quadratic (rather than linear) functions of i. It is clear that the performance of the fin is considerably changed. This not only demonstrates the subtlety of lift-based propulsion but also brings in more parameters to be optimized for the design of future biomimetic devices.

As mentioned in the introduction, in drag-based swimming (rowing mode) with flexible fins, the duty factor of swimming reaches 1 (Mittal et al., 2006; Tangorra et al., 2008). However, the studies by Ramamurti et al. (Ramamurti et al., 2002) as well as our current simulation of lift-based swimmers (in flapping mode) predict duty factors smaller than 1. This may be attributed to the following factors: (1) these studies were carried out at different forward speeds. As indicated by Tangorra et al. (Tangorra et al., 2008), as forward speed increases (with other parameters fixed) the capacity of thrust generation decreases and this may eventually generated a lower than 1 duty factor. (2) It appears that structural flexibility has a larger effect on the performance of a rowing fin. Indeed in the rowing mode the duty factor of 1 is only achieved with a highly flexible fin. To quantitatively understand this effect, future investigations using fins with different levels of flexibility are required. (3) The sequences of vortex shedding (dorsal/ventral edge vortices in flapping mode *vs* dorsal/ventral edge vortices along with abduction/adduction tip vortices in rowing mode) are different between flapping and rowing modes. These differences may affect the thrust drop during the transition from downstroke (instroke) to upstroke (outstroke) motions and consequently the duty factor.

One of the key characteristics of the current study is the incorporation of a LEV model. As suggested by our results, two concentrations of vorticity, one generated during the downstroke motion and the other during the upstroke motion, are shed from the leading edge into the wake. LEV significantly affects the thrust generation and propulsion efficiency of the fin. The current model of LEV stems from the potential flow framework. At a result, although this method provides a convenient alternative to the Navier–Stokes equations, it is based upon simplified descriptions of the otherwise complicated mechanisms involved in vorticity shedding, vortex formation and vortex–body interactions. For example, as indicated in our recent Navier–Stokes study (Zhu and Peng, 2009), when the vortex shedding and the body motion are properly synchronized, the energy of LEV can be effectively recovered so that the performance of the system is enhanced. For accurate prediction and comprehensive understanding of mechanisms like this and their effects upon the dynamical performance of the fin, more sophisticated solvers (e.g. those based on Navier–Stokes equations) are necessary. Although these models are expected to be more accurate, they are computationally expensive so that it is critical to carefully choose the cases to be tested. The highly efficient potential-flow-based simulations discussed in this study can provide valuable guidance.

LIST OF ABBREVIATIONS

A	cross-sectional area of a ray
BEM	boundary-element method
$C_T(\bar{C}_T)$	(mean) thrust coefficient
$C_L[C_L^{(1)}]$	(first-harmonic) lift coefficient
$C_y[C_y^{(1)}]$	(first-harmonic) lateral force coefficient
d	thickness of the fin
D	material damping coefficient of the rays
E	Young's modulus of the rays
EA	tensile stiffness
EI	bending stiffness
$\mathbf{F}$	hydrodynamic force on the fin
F_c	constraining force from the membrane that controls the distance between the neighboring rays
$\mathbf{F}_h$	hydrodynamic force on a ray
$F_T(\bar{F}_T)$	(mean) thrust force
F_y	lateral force
F_z	lift force
GJ	torsional stiffness
L	length of ray
LEV	leading edge vortices
L_i	length of Ray i
L_1	length of Ray 1 (the leading edge ray)
M	mass per unit length
$\mathbf{M}$	internal moment
$\mathbf{n}$	unit normal vector pointing into the fin
N_b	number of panels on the fin surface
N_w	number of panels on the wake
p	hydrodynamic pressure
$P(\bar{P})$	(mean) power spent
Re	Reynolds number
s	distance from a point on a ray to the basal end measured along the unstretched ray
S_b	fin surface
S_t	Strouhal number
S_w	wake surface
U	forward speed
t	time
T	period ($2\pi/\omega$)
$\mathbf{T}$	internal force inside a ray
$\mathbf{V}$	translational velocity of a ray
$\mathbf{V}_b$	instantaneous velocity at the surface of the fin
x_0	length of baseline
(x, y, z)	global coordinate system
α_0	maximum angle of rolling of each ray in one stroke
α_I	angle between base end of Ray i and the x–z plane
ε	strain in a ray
η	propulsion efficiency
θ_i	angle between base end of Ray i and the x-axis
ρ	density of water

$(\boldsymbol{\tau}, n, b)$	tangential, normal and bi-normal unit vectors in the Lagragian coordinate system
φ	phase of the i-th ray in rolling
Φ	flow potential
ω	frequency
$\boldsymbol{\omega}$	angular velocity of a ray
$\boldsymbol{\Omega}$	Darboux vector measuring material torsion and curvatures of a ray

REFERENCES

Alben, S., Madden, P. G. and Lauder, G. V. (2007). The mechanics of active fin-shape control in ray-finned fishes. *J. R. Soc. Interface* **4**, 243-256.

Anderson, J. M., Streitlien, K., Barrett, D. S. and Triantafyllou, M. S. (1998). Oscillating foils of high propulsive efficiency. *J. Fluid Mech.* **360**, 41-72.

Archer, R. D., Sapuppo, J. and Betteridge, D. S. (1979). Propulsion characteristics of flapping wings. *Aeronaut. J.* **83**, 355-371.

Blake, R. W. (1979). The mechanics of labriform locomotion. I. Labriform locomotion in the angelfish *(Pterophyllum eimekei):* an analysis of the power stroke. *J. Exp. Biol.* **82**, 255-271.

Blake, R. W. (1981). Mechanics of drag-based mechanisms of propulsion in aquatic vertebrates. *Symp. Zool. Soc. Lond.* **48**, 29-52.

Blake, R. W. (1983). *Fish Locomotion.* Cambridge: Cambridge University Press.

Dong, X. (2007). Boundary element simulation of oscillating foil with leading-edge separation. Msc Thesis, Massachusetts Institute of technology, Cambridge, MA.

Drucker, E. G. and Jensen, J. S. (1996a). Pectoral fin locomotion in the striped surfperch. I. Kinematic effects of swimming speed and body size. *J. Exp. Biol.* **199**, 2235-2242.

Drucker, E. G. and Jensen, J. S. (1996b). Pectoral fin locomotion in the striped surfperch. II. Scaling swimming kinematics and performance at a gait transition. *J. Exp. Biol.* **199**, 2243-2252.

Drucker, E. G. and Jensen, J. S. (1997). Kinematic and electromyographic analysis of steady pectoral fin swimming in the surfperches. *J. Exp. Biol.* **200**, 1709-1723.

Drucker, E. G. and Lauder, G. V. (2003). Function of pectoral fins in rainbow trout: behavioral repertoire and hydrodynamic forces. *J. Exp. Biol.* **206**, 813-826.

Faltinsen, O. M. and Pettersen, B. (1987). Application of a vortex tracking method to separated flow around marine structures. *J. Fluids Struct.* **1**, 217-237.

Gibb, A. C., Jayne, B. C. and Lauder, G. V. (1994). Kinematics of pectoral fin locomotion in the bluegill sunfish *Lepomis macrochirus. J. Exp. Biol.* **189**, 133-161.

Harder, W. (1975). *Anatomy of Fishes.* Stuttgart: E. Schweizerbart'sche Verlagsbuchhandlung.

Jones, M. A. (2003). The separated flow of an inviscid fluid around a moving flat plate. *J. Fluid. Mech.* **496**, 405-441.

Junkins, J. L. and Turner, J. D. (1986). *Optimal Spacecraft Rotational Maneuvers.* Amsterdam: Elsevier.

Kardong, K. V. (1998). *Vertebrates: Comparative Anatomy, Function, Evolution.* 2nd edn. Dubuque: W. C. Brown.

Kato, N. (1999). Hydrodynamic characteristics of mechanical pectoral fin. *ASME J. Fluids Eng.* **121**, 605-613.

Katz, J. (1980). A discrete vortex method for the non-steady separated flow over an airfoil. *J. Fluid Mech.* **102**, 315-328.

Katz, J. and Plotkin, A. (1991). *Low-Speed Aerodynamics: From Wing Theory to Panel Methods.* New York: McGraw-Hill.

Katz, J. and Weihs, D. (1978). Hydrodynamic propulsion by large amplitude oscillation of an airfoil with chordwise flexibility. *J. Fluid Mech.* **88**, 485-497.

Lauder, G. V. and Drucker, E. G. (2004). Morphology and experimental hydrodynamics of fish fin control surfaces. *IEEE J. Ocean Eng.* **29**, 556-571.

Lauder, G. V. and Jayne, B. C. (1996). Pectoral fin locomotion in fishes: testing drag-based models using three-dimensional kinematics. *Am. Zool.* **36**, 567-581.

Lauder, G. V., Madden, P. G. A. (2007). Fish locomotion: kinematics and hydrodynamics of flexible foil-like fins. *Exp. Fluids* **43**, 641-653.

Lauder, G. V., Madden, P. G. A., Mittal, R., Dong, H. and Bozkurttas, M. (2006). Locomotion with flexible propulsors I: experimental analysis of pectoral fin swimming in sunfish. *Bioinspir. Biomim.* **1**, S25-S34.

Mittal, R., Dong, H., Bozkurttas, M., Lauder, G. V. and Madden, P. (2006). Locomotion with flexible propulsors: II. computational modeling of pectoral fin swimming in sunfish. *Bioinspir. Biomim.* **1**, 35-41.

Ramamurti, R., Sandberg, W. C., Lohner, R., Walker, J. A. and Westneat, M. (2002). Fluid dynamics of flapping aquatic flight in the bird wrasse: three-dimensional unsteady computations with fin deformation. *J. Exp. Biol.* **205**, 2997-3008.

Read, D. A. (2000). Oscillatory foil for propulsion and maneuvering of ships and underwater vehicles. Msc Thesis, Massachusetts Institute of technology, Cambridge, MA, USA.

Standen, E. M. (2008). Pelvic fin locomotor function in fishes: three-dimensional kinematics in rainbow trout (*Oncorhynchus mykiss*). *J. Exp. Biol.* **211**, 2931-2942.

Taneda, S. (1977). Visual study of unsteady flows around bodies. *Prog. Aerosp. Sci.* **17**, 287-348.

Tangorra, J. L., Davidson, S. N., Hunter, I. W., Madden, P. G. A., Lauder, G. V., Dong, H., Bozkurttas, M. and Mittal, R. (2007). The development of a biologically inspired propulsor for unmanned underwater vehicles. *IEEE J. Ocean Eng.* **32**, 533-550.

Tangorra, J. L., Lauder, G. V., Madden, P. G., Mittal, R., Bozkurttas, M. and Hunter, I. W. (2008). A birobotic flapping fin for propulsion and maneuvering. *Proc. IEEE Int. Conf. Robot. Autom.* 700-705.

Thorsen, D. H. and Westneat, M. W. (2005). Diversity of pectoral fin structure and function in fishes with labriform propulsion. *J. Morphol.* **263**, 133-150.

Tjavaras, A. A. (1996). The dynamics of highly extensible cables. PhD Thesis, Massachusetts Institute of Technology, Cambridge, MA, USA.

Tjavaras, A. A., Zhu, Q., Liu, Y., Triantafyllou, M. S. and Yue, D. K. P. (1998). The mechanics of highly-extensible cables. *J. Sound Vib.* **213**, 709-737.

Vogel, S. (1994). *Life in Moving Fluids: The Physical Biology of Flow*, 2nd edn. Princeton, NJ: Princeton University Press.

Walker, J. A. and Westneat, M. (1997). Labriform propulsion in fishes, kinematics of flapping aquatic flight in the bird wrasse *Gomphosus varius* (labridae). *J. Exp Biol.* **200**, 1549-1569.

Walker, J. A. and Westneat, M. (2002). Kinematics, dynamics, and energetics of rowing and flapping propulsion in fishes. *Integr. Comp. Biol.* **42**, 1032-1043.

Webb, P. W. (1973). Kinematics of pectoral fin propulsion in *Cymatogaster aggregata*. *J. Exp. Biol.* **59**, 697-710.

Westneat, M. (1996). Functional morphology of aquatic flight in fishes: mechanical modeling, kinematics, and electromyography of labriform locomotion. *Am. Zool.* **36**, 582-598.

Zhu, Q. (2007). Numerical simulation of a flapping foil with chordwise or spanwise flexibility. *AIAA J.* **45**, 2448-2457.

Zhu, Q. and Shoele, K. (2008). Propulsion performance of a skeleton-strengthened fin. *J. Exp. Biol.* **211**, 2087-2100.

Zhu, Q. and Peng, Z. (2009). Mode coupling and flow energy harvesting by a flapping foil. *Phys. Fluids* **21**, 033601.

Zhu, Q., Wolfgang, M., Yue, D. K. P. and Triantafyllou, M. S. (2002). Three-dimensional flow structures and vorticity control in fish-like swimming. *J. Fluid Mech.* **468**, 1-28.